Revealing a High Water Abundance in the Upper Mesosphere of Mars with ACS onboard TGO

Denis A. Belyaev[1], Anna A. Fedorova[1], Alexander Trokhimovskiy[1], Juan Alday[2], Franck Montmessin[3], Oleg I. Korablev[1], Franck Lefèvre[3], Andrey S. Patrakeev[1], Kevin S. Olsen[2], and Alexey V. Shakun[1]

[1]Space Research Institute (IKI), Moscow, Russia.

[2]Department of Physics, University of Oxford, UK.

[3]LATMOS/CNRS, Paris, France.

Corresponding author: Denis Belyaev (dbelyaev@iki.rssi.ru)

Key Points:

- For the first time, water relative abundances are reported in a previously unexplored altitude range: from 100 to 120 km
- Both the global dust storm (MY34) and the two perihelion seasons (MY34, 35) observed reveal 10–50 parts of H_2O per million by volume at 100–120 km
- Contributions of a single GDS and perihelion into the H escape from Mars are nearly equivalent, suggesting the repeatable seasonal effect dominates in the long term

Abstract

We present the first water vapor profiles encompassing the upper mesosphere of Mars, 100–120 km, far exceeding the maximum altitudes where remote sensing has been able to observe water to date. Our results are based on solar occultation measurements by Atmospheric Chemistry Suite (ACS) onboard the ExoMars Trace Gas Orbiter (TGO). The wavelength range observed (~2.7 μm) possesses strong CO_2 and H_2O absorption lines allowing sensitive temperature and density retrievals. We report the maximum H_2O mixing ratio varying from 10 to 50 ppmv at 100–120 km during the global dust storm of MY34 and around southern summer solstice of Martian Years (MY) 34 and 35. During other seasons water remains below 2-3 ppmv. The high values above 100 km establish a bridge between the regular water enrichment observed below (60-100 km) and the atomic hydrogen escaping from the exosphere.

Plain Language Summary

We report regular events of high abundances of the water vapor (H_2O) in the upper atmosphere of Mars (100–120 km). So far, any water enrichment has not been revealed by remote sensing at such high altitudes. Higher than 80 km, solar light breaks water vapor molecules into H and O atoms, which may reach the exosphere and escape the planet. When Mars is closer to the Sun (the perihelion season), the atmosphere's circulation intensifies, causing increased dust activity with global dust storms (GDS), occurring every 3–4 Mars years. We observed during the second halves of Martian years 34 and 35 (2018–2020), including one GDS and two perihelion seasons. We report that the maximum water relative abundance reaches 10–50 parts per million in volume (ppmv) at 100-120 km during the GDS and every perihelion season. These high values indicate that the Martian atmosphere above 100 km regularly hosts large amounts of water, facilitating the long-term escape of water from the planet.

1 Introduction

The vertical distribution of water vapor (H_2O) on Mars is an indicator of the intricate coupling of distinct phenomena: temperature variations, cloud formation, sublimation, turbulent and convective mixing, etc. H_2O is usually expected to be confined below the hygropause, which is the level where the saturation condition is met and where water ice clouds may form, as occurs on Earth. For the first time, this layer was established on Mars by ground-based microwave soundings of Clancy et al. (1996) with a saturation level between 10–20 km around the aphelion, i.e., Solar Longitudes (L_S) 70°, and 40–60 km around perihelion (L_S 250°). In parallel, Rodin et al. (1997) reported water vapor profiles retrieved from the solar occultations made by Auguste on Phobos-2 in 1989. The existence of a hygropause at 30–35 km (with a mixing ratio of 3 ppm) in the northern spring (L_S=0°–20°) near the equator was claimed. The first climatology of water vapor profiles was derived from SPICAM-IR solar occultations on Mars Express (MEx) (Fedorova et al., 2009; 2018; 2021; Maltagliati et al., 2013), covering eight Martian years. The hygropause level was found to vary from 40 to 80 km depending on season, latitude, and dust events.

The observation of large amounts of water vapor in and above the middle atmosphere (>40 km) was accompanied by the discovery of fast variations of the hydrogen corona over several weeks (Chaffin et al., 2014; Clarke et al., 2014). This variability suggested a new paradigm in the perception of how water escapes from Mars (Chaffin et al., 2017). So far, water escape was thought to be controlled by a slow process involving H_2, formed from the catalytic recombination of carbon dioxide with odd hydrogen (McElroy and Donahue, 1972; Krasnopolsky, 2002). The non-condensable H_2 can overcome the hygropause and reach the mesosphere (80–120 km) transported by turbulent mixing or circulation. There it can dissociate and release H atoms that will escape the planet once above the exobase.

Long-term observations revealed that water vapor transport from the troposphere into the lower mesosphere of Mars occurs during major dust storms. In particular, a significant H_2O enhancement in the middle atmosphere was observed during the global dust storm (GDS) in 2007 (MY28) with a rise of the hygropause altitude to >60 km (Fedorova et al., 2018; Heavens et al., 2018). Sensitive solar occultation measurements by NOMAD and ACS NIR instruments onboard the ExoMars Trace Gas Orbiter (TGO) showed water reaching 80–100 km (Aoki et al., 2019; Fedorova et al., 2020) during two storms in 2018-2019 (the global one at L_S 190°–220° and the regional one at L_S 330° in MY34; Montabone et al., 2020). Fedorova et al. (2020) revealed the water supersaturation at 70–90 km even in the presence of H_2O ice clouds not only during the GDS but also near the Southern summer solstice (L_S~270^o) when water reached 90-100 km as well. Altogether, these studies promote a new mechanism for controlling H_2O escape through direct delivery to above 80 km and further photodissociation (Chaffin et al., 2017; Krasnopolsky et al., 2019). The only general circulation model describes an upward water flux into the thermosphere (>120 km) for the GDS scenario (Shaposhnikov et al., 2019). They predict high water volume mixing ratio (VMR) values: ~100 ppm at 100 km and ~200 ppm at 150 km for the southern middle latitudes.

The discussion regarding a relative contribution of perihelion or GDS to the mesospheric water enrichment was recently fed by SPICAM/MEx long-term observations covering Martian Years 28 through 35. Here, Fedorova et al. (2021) claimed a regular rise of water abundance up to 80–90 km in perihelion, which is compatible with GDS quantities. The new ACS/TGO dataset confirms those conclusions for altitudes below 100 km in MY34–MY35 (Fedorova et al. 2020, Alday et al., 2021). In parallel, during the perihelion season, the D/H ratio in water decreases with altitude from 4–6 times SMOW (Standard Mean Ocean Water) in the lower atmosphere to 2–3 times in the middle one (50-70 km) as measured by ACS MIR (Alday et al., 2021) and NOMAD (Villanueva et al., 2021) spectrometers. Alday et al. (2021) show that ultraviolet H_2O photolysis dominates the production of H relative to D atoms in the upper atmosphere.

From above, ion chemistry in the thermosphere has been characterized by the NGIMS mass-spectrometer on MAVEN (Benna et al., 2015) and interpreted by the ionospheric model of Fox et al. (2015). Using NGIMS data, Stone et al. (2020) measured H_2O ion concentrations around ~150 km for the 2014–2018 period (MY32–MY34). With the help of the model by Fox et al., the relative abundance of water at this altitude on the dayside was found to vary seasonally from 2 to 5 ppm. Several enhanced dusty episodes disrupt this seasonal signal: 7–9 ppm during the regional storm of MY32, 10–20 ppm in the southern summer of MY33, and up to 60 ppm in the GDS of MY34. Stone et al. (2020) concluded that water transport into the ionosphere and its destruction are the main mechanisms in the overall hydrogen escape from Mars.

We used the data of the middle infrared spectrometer of the Atmospheric Chemistry Suite (ACS MIR) onboard the ExoMars TGO, which measures water vapor VMR and atmospheric density in a wide range of altitudes, from the troposphere to the lower thermosphere, using the strong absorption bands of H_2O and CO_2 around 2.66–2.70 μm. A high spectral resolution and a good signal-to-noise ratio of ACS MIR allows the measurements of water profiles up to 120 km, the altitude unreachable for the ACS NIR, and SPICAM spectrometers, sensing the 1.38 μm absorption band (Fedorova et al., 2020; 2021). The strong H_2O absorption around 2.6 μm is also used by NOMAD, yielding water profiles up to ~90 km (Aoki et al., 2019; Villanueva et al., 2021).

Here we report the first water vapor abundance measurements in the upper mesosphere (up to 120 km) of Mars. The goal of our paper is to compare the mesospheric water behavior between the second halves of MY34 and MY35 when the high H_2O content is observed. We aim to clarify the dominant role of H_2O delivery to the upper mesosphere: either it belongs to sporadic dust events (GDS or a strong regional storm) or it also occurs regularly, every martian year, around Southern summer solstice. For that, we analyze seasonal and latitudinal variations of H_2O VMR vertical profiles retrieved from the ACS MIR solar occultation experiment.

2 Measurements and dataset overview

2.1 ACS MIR spectroscopy and retrievals

ACS MIR, a solar occultation cross-dispersion echelle spectrometer, records spectra from a set of adjacent diffraction orders (from 10 to 20 per occultation) projected onto a 2D detector array (Korablev et al., 2018). To retrieve high altitude water vapor abundances together with the atmospheric temperature and pressure, we use MIR spectra from the diffraction order #223. They cover a narrow wavelength interval of 2.66–2.68 μm (3733–3753 cm^{-1}), including a part of the 2.7-μm CO_2 absorption band and a few strong H_2O lines near 2.66 μm (Fig. 1a, 1b, Fig. S1). The instrument's spectral resolution is ~0.15 cm^{-1}, while the signal-to-noise ratio ranges from 2,000 to 4,000, which provides high sensitivity for detections in the upper atmosphere where atmospheric constituents are low. Temperature (Fig. 1c) is retrieved by fitting a synthetic model to the CO_2 rotational band taking advantage of its temperature dependence under the assumption of hydrostatic equilibrium. This procedure was applied iteratively, with feedback of the retrieved temperature to the model. The temperature measurements were then validated against those made by MIR near the 2.6 μm CO_2 band (Alday et al., 2019) and by ACS NIR around the 1.58 μm band (Fedorova et al., 2020). As a result, one occultation session allows us to simultaneously retrieve profiles of pressure and temperature (from CO_2 absorption bands) and the H_2O number density (Fig. 2c). The water abundance can then be expressed relative to the total atmospheric density, that is, in VMR (in ppmv). Specific details of the algorithms pertaining to this work can be found in the Supporting Information.

The dataset analyzed here consists of a series of transmission spectra obtained during a solar occultation while the line of sight of the instrument progressively penetrates from the upper into deeper layers of the atmosphere, or vice versa (see examples in Fig. 1a, 1b). The transmission is determined as the solar spectrum ratio measured through the atmosphere to the reference one, taken from the data above a tangential height of 200 km. This altitude level is negligibly attenuated by the atmosphere even within the very strong CO_2 band system at 2.7 μm. The typical integration time is 2 seconds that provides an altitude resolution ranging from 0.5 to 2.5 km, depending on the occultation duration. It gives sufficiently fine vertical sampling for an atmosphere whose scale height ranges from 5 to 10 km depending on temperature. The ACS MIR field of view projected at the limb is estimated to be around 1-3 km in altitude equivalent.

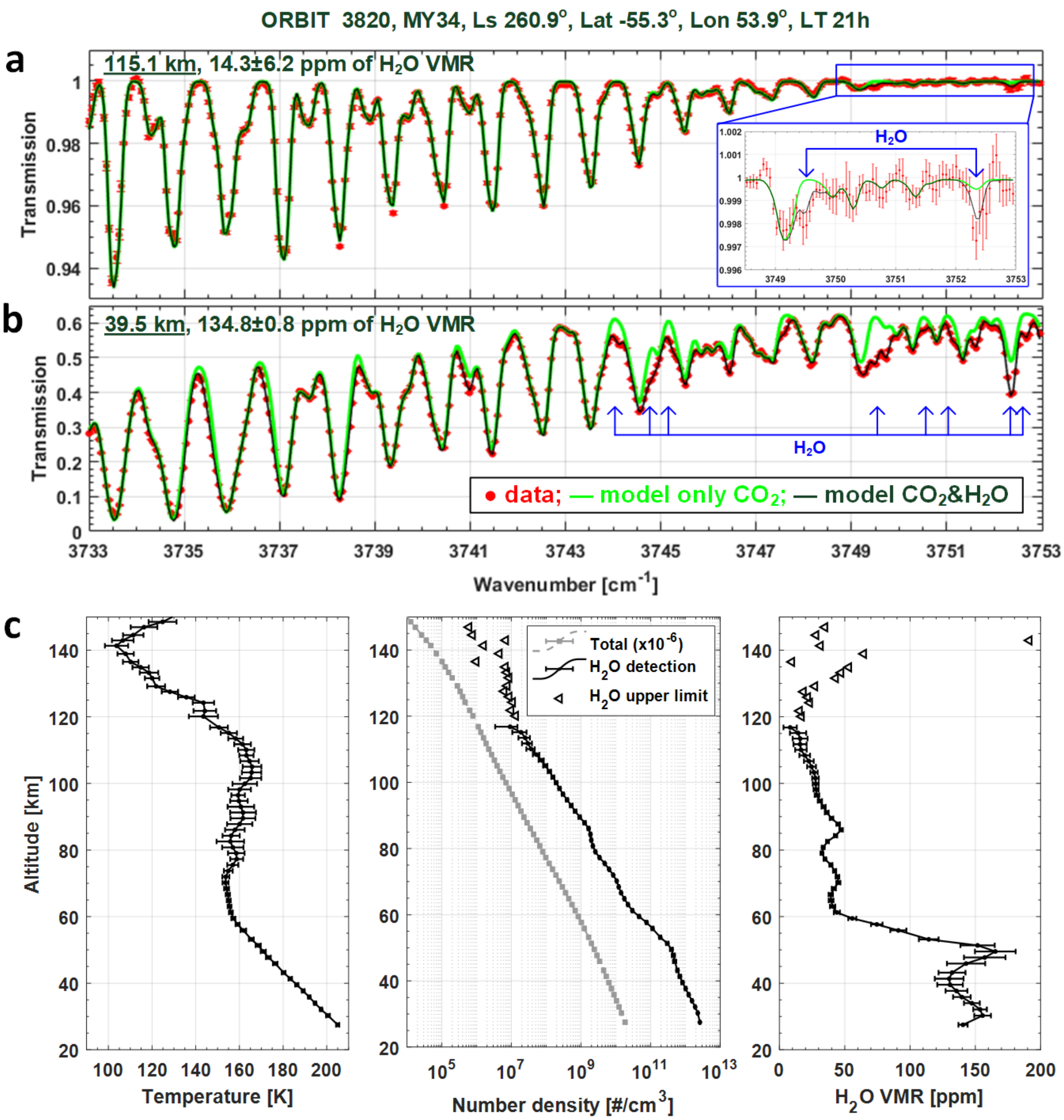

Figure 1. Example ACS MIR spectra and profiles of the retrieved quantities. Measured transmission spectra (red) at tangent altitudes of 115.1 km (**a**) and 39.5 km (**b**) are compared with the best-fit models, including both CO_2 and H_2O absorptions (black), and only CO_2 absorption (green). Blue arrows indicate water absorption lines. Zoom in (**a**) shows a part with the strongest H_2O absorption detected at 115 km. (**c**) Retrieved vertical profiles of temperature (left), number densities (center), and H_2O volume mixing ratio (VMR) (right). Black triangles mark H_2O upper limits (see Supporting Information for the description of uncertainties).

2.2 Data selection

To reveal the upper mesospheric water we focused on the second halves of MY34 and MY35, which correspond to ACS MIR observations from May 2018 to March 2019 and from April 2020 to January 2021. The selected dataset comprises 187 occultation sessions in the

Northern Hemisphere and 156 sessions in the Southern Hemisphere, encompassing seasonal periods from L_S 180° to 355° in MY34 and from L_S 185° to 356° in MY35 (Fig. 2a). Figure 2a shows the latitude coverage with the corresponding aerosol activity, which was defined for each occultation as an altitude level where the slant opacity equals 0.3 (~0.75 of the atmospheric transmittance in the continuum). Measurements in the Northern Hemisphere occurred mostly in the mid-latitude range, which is between 40°N and 70°N. In the South, occultations before, during the GDS (L_S<230°), and around the regional storm of MY34 (L_S 320°–330°) were performed close to the polar region (60°S–90°S), while perihelion observations (L_S 270°) were made in mid-latitudes. Only a few sessions occurred in the equatorial region at L_S~240° and L_S~300° of MY34 and at L_S~210° and L_S~280° of MY35. These observations are accompanied by a higher aerosol loading than those, which are close to the Poles (Fig. 2a). The overall map of the MY34 dust climatology can be found in (Montabone et al., 2020).

3 Seasonal variation of altitude profiles

Observations in the second half of MY34 and MY35 uncover events, which drastically perturbed the temperature and water vapor vertical distributions. The peculiar pattern to compare with is the MY34 GDS and perihelion periods in MY34 versus MY35, which had no GDS but a regular dust activity in its second half. The seasonal variation of the processed altitude profiles is presented in Figure 2(b,c). We binned the profiles into intervals of 2° in solar longitude (L_S) and 2 km in altitude. Depending on the L_S and altitude sampling, the value in each bin is calculated as the weighted mean of one to five individual points. We excluded all points with uncertainties exceeding 20 K in temperature and 1-sigma in the H_2O mixing ratio. The second rejection criterion corresponds to the detection limit (~10^7 cm^{-3}) of water number density (see in Fig. 1c) that defines the seasonal variations of the uppermost detectable points in Figure 2c.

We observe temperature (Fig. 2b) and H_2O (Fig. 2c) peaking in the middle atmosphere (40–80 km) during the GDS of MY34, L_S 190°–220°, and an additional smaller peak at L_S 320°–330°, corresponding to a regional storm. Moreover, the rise of water vapor to higher altitudes, up to the mesopause at 110–130 km where temperature encounters a minimum, is observed during two perihelion intervals (L_S 250°–290°) of MY34 and MY35. Here, the Southern summer (Fig. 2c, right panel) is accompanied by a more humid mesosphere (40–60 ppm of H_2O) than the Northern Winter (Fig. 2c, left panel) where the mean mesospheric water reaches 20–30 ppmv on average between 80 and 120 km. On the contrary, out of the perihelion peak or dust events, i.e. for the selected data at the beginning of the MY34 GDS and at the very end of MY 34, 35, water content above 80 km never exceeds 2-3 ppmv.

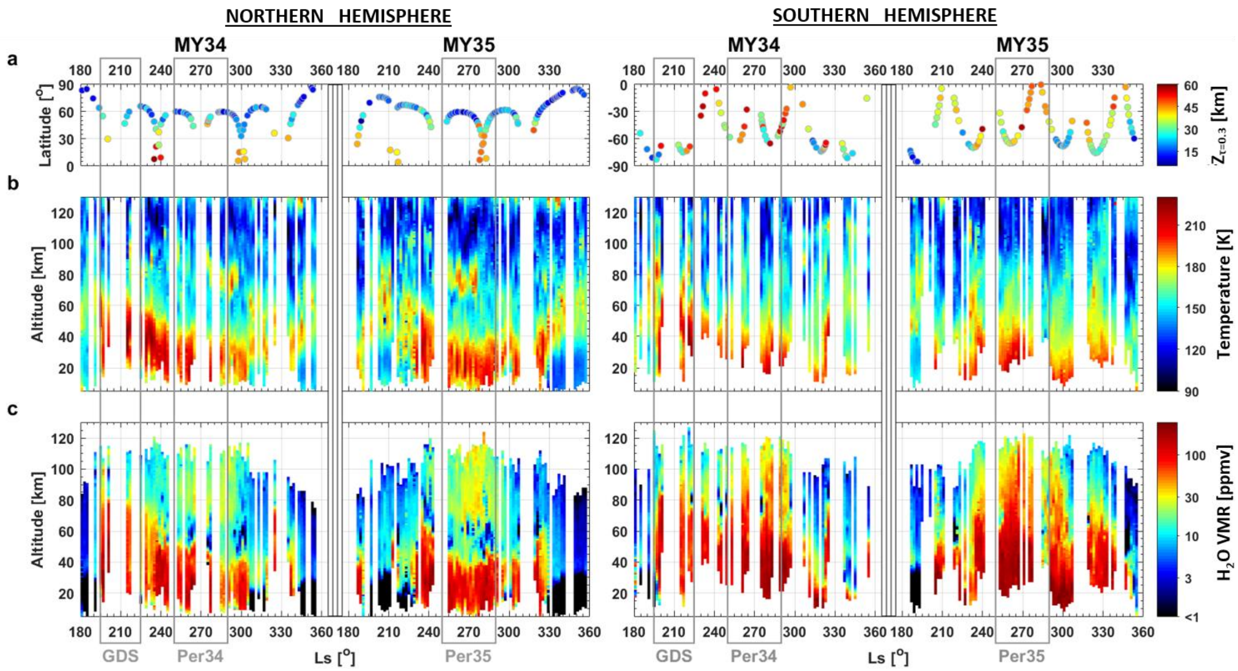

Figure 2. Seasonal map of atmospheric temperature and H_2O mixing ratio during the second half of MY34 and MY35. The data are plotted in function of L_S and altitude for the Northern (left) and the Southern (right) hemispheres. (**a**) Latitudinal distribution of the ACS-MIR solar occultations, depending on an altitude level where the aerosol slant opacity (τ) equals 0.3. (**b**) Temperature. (**c**) Volume mixing ratio (VMR) of water vapor. Grey frames outline time intervals of the global dust storm (GDS) in MY34 and the two perihelions in MY34 (Per34) and MY35 (Per35).

4 H_2O variations around perihelion

To quantify seasonal trends of water content in the mesosphere, we selected three altitude layers corresponding to 80 km, 100 km, and 110–120 km. The first layer, which corresponds to the lower mesosphere, is accessible in all profiles (Fig. 2c) when the vapor concentration exceeds the detection limit of ~10^7 cm^{-3}, even in low water loading periods. A value of H_2O VMR at 80 km could be derived in every individual altitude profile when interpolating between adjacent points below and above this level. The water content at 100 km was found similarly, though based on a smaller number of profiles. Water at 110–120 km, in the upper mesosphere, shows up only in stormy periods and around perihelion (Fig. 2c).

Observed variations during perihelion for the three selected levels are presented in Figure 3 for both Martian Years. The number of MIR observations at Position #4 is low during the stormy events of MY34. Nevertheless, a comparison with MY35 reveals a significant excess of H_2O mixing ratio during the GDS: by a factor of 6–8 at 80 km (Fig. 3c) and by a factor of 3–5 at 100-120 km from L_S 190° to 220° (Fig. 3a, 3b). A surge at L_S 320°–330° reveals the effect of the regional dust storm of MY34, which delivers far less water into the mesosphere than the GDS. Around the perihelion, L_S=240°–300° water behaves almost identical between MY34 and MY35. For both Martian Years, the maximum H_2O mixing ratio was observed near the Southern summer solstice (L_S~270°), reaching values of 40–80 ppm at 80 km, 30–60 ppm at 100 km, and 20–50 ppm at 110–120 km. In the Northern winter solstice, it varied from 20 to 40 ppm at all levels, 80 through 120 km. We compare our results at 80 km with the corresponding ACS NIR dataset derived from the MY34 profiles of Fedorova et al. (2020). The NIR dataset is five times denser than used in the present work, and it observed the H_2O variations in greater detail, especially during the dust events of MY34.

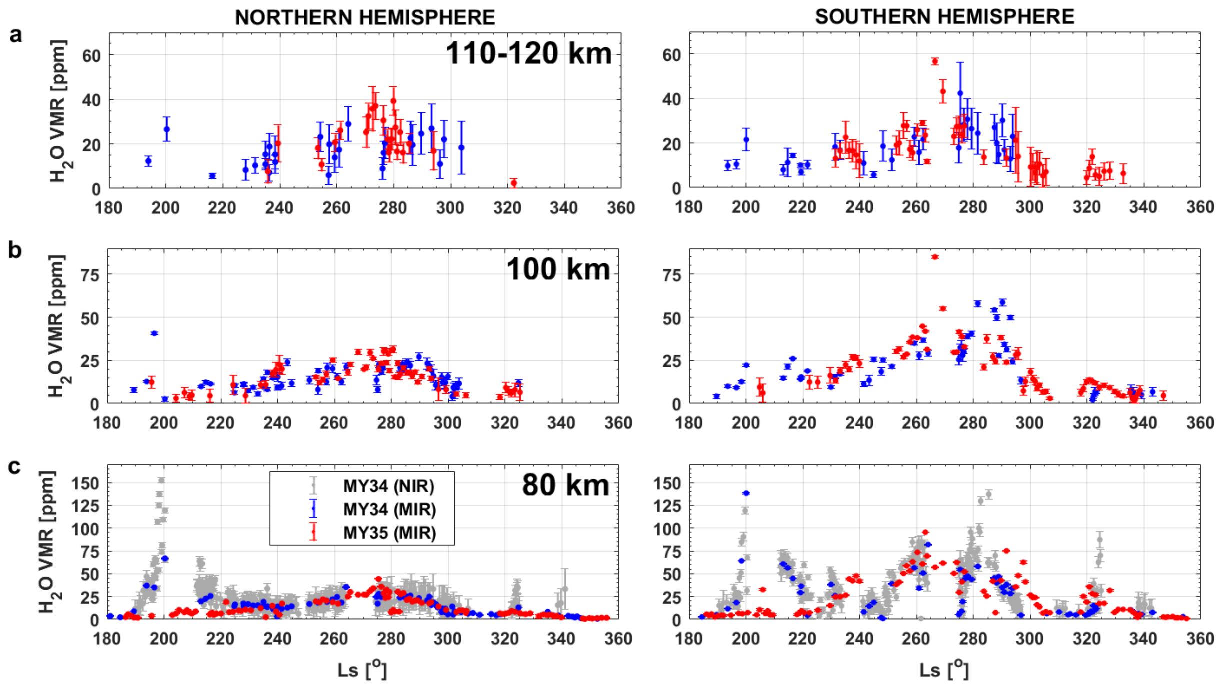

Figure 3. Seasonal trends of H_2O volume mixing ratio (VMR) at three altitude levels, 80, 100, 120 km. The season is the second half of MY34 (in blue) and of MY35 (in red). Each point corresponds to an individual vertical profile: weighted mean value obtained in between 110-120 km (**a**), and interpolated value for the levels of 100 km (**b**) and 80 km (**c**). Data at 80 km in grey (**c**) are taken from the ACS NIR profiles (Fedorova et al., 2020).

4 Discussion and Conclusions

For the first time, we report observations of H_2O relative abundances in a previously unexplored altitude range (from 100 to 120 km). There we find 10–30 ppm of water vapor during the MY34 GDS and 20–50 ppm around the perihelion point (L_S=250°–290°) of MY34 and MY35 in both hemispheres. Our stormy retrievals at 100–120 km are of the same order of magnitude as MAVEN NGIMS results reported by Stone et al. (2020) at ~150 km. Surprisingly, NGIMS water relative abundances reveal a mission-wise maximum of H_2O at 150 km during the MY34 GDS, whereas we repeatedly observe the annual maximum around the Southern summer solstice both in MY34 and MY35.

NGIMS measures ions from which neutral H_2O VMRs at 150 km were derived and injected into a 1D photochemical model. The model was adjusted to reproduce the H_2O abundance at 150 km inferred from the [H_2O^+] ions measured by NGIMS under two scenarios: low water, corresponding to 2 ppm prescribed at 80 km in a non-GDS case; and high water, of 40 ppm in a GDS case (Stone et al., 2020; as corrected in March 2021). Notably, all the solar occultation observations performed by TGO and MEX to date (Fedorova et al., 2018, 2020, 2021; Aoki et al., 2019; Villanueva et al., 2021), including the present dataset (Fig. 3a), report even higher water vapor VMRs, of 50–80 ppm during the GDS. Stone et al. (2020) indicate a systematic uncertainty of 69% on their neutral H_2O inference, which brings MAVEN, TGO, and MEX values to an agreement within error bars.

It is important to consider how ACS's high altitude water vapor abundances combine with photolysis since this process has been hypothesized to be essential, if not the dominant, source for the H atoms observed in the exosphere (Chaffin et al., 2017). The conclusion of Stone et al. (2020) insists on the GDS's predominance and related ion chemistry in the H atoms' production. Our observations suggest that while the GDS period corresponds to the maximum of water abundance at 80 km, H_2O at 120 km peaks only later, at the Southern summer solstice, when it is twice as large as during the GDS. This enhanced solstice maximum suggests that relative water abundance declines more rapidly above 80 km during the GDS than after, during perihelion (Fig. 4).

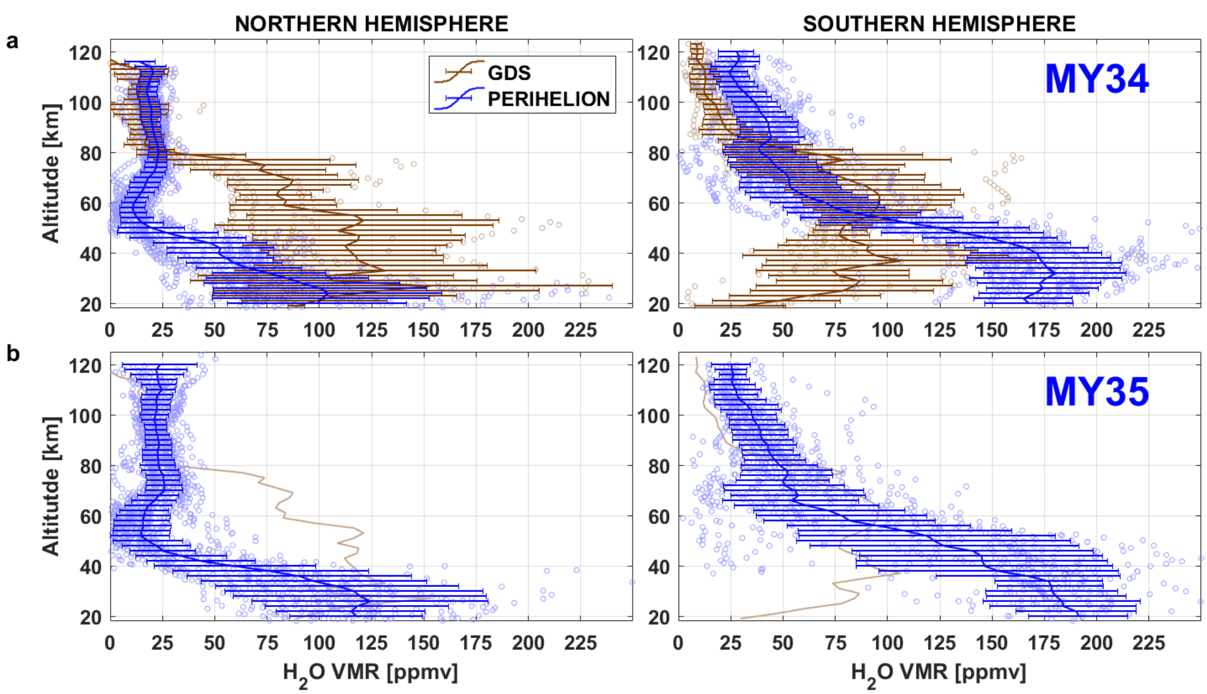

Figure 4. Altitude profiles of average H_2O volume mixing ratio (VMR) during the GDS (MY 34) and the perihelion season (MY 34, 35). The dataset used includes all ACS MIR observations highlighted in Fig. 2: GDS of MY34 (L_S=195°–220°), brown average curve, and individual MIR detections; the bin around the perihelion point (L_S=250°–295°) (blue). Upper panels: MY34 (**a**); lower panels: MY35 (**b**). The left and right panels are for the Northern and Southern hemispheres. Averaged profiles are presented with 1-sigma dispersion over 2-km altitude bins. The GDS curves are also indicated for MY35 to facilitate comparison.

In Figure 4, we combined altitude profiles from GDS-only (L_S 195°–220°) and perihelion (L_S 250°–295°) intervals to compare averaged vertical trends between them and to estimate an integral escape flux of the atomic hydrogen in each case. For that, we applied the model of Chaffin et al. (2017), which predicts the atmospheric escape rate depending on the water injection into different altitudes (see Figure 3 of their paper). Our rough calculations show that the H escape flux is about 5.7×10^{9} cm^{-1}s^{-1} during GDS for both hemispheres, while around perihelion point it is 4.0×10^{9} cm^{-1}s^{-1} for the Northern Hemisphere and 6.0×10^{9} cm^{-1}s^{-1} for the

Southern one in both Martian Years. These values were derived when integrating the flux over altitudes from 20 to 120 km and in time intervals of 25 sols for GDS (L_S 195°–220°) and 45 sols for perihelion (L_S 250°–295°). Thus, we claim nearly equivalent contributions from a single GDS and the perihelion period into the hydrogen escape by the high water enrichment in the middle/upper atmosphere. Fedorova et al. (2021) come to a similar conclusion based on SPICAM/MEx water profiles up to 80 km. A GDS occurs every 3–4 martian years on average (Zurek and Martin, 1993; Wang and Richardson, 2015), and the yearly perihelion contribution to the hydrogen escape should prevail by a factor of ≥3.5. Moreover, the enhanced circulation and heating of the atmosphere in perihelion driven by the hemispheric dichotomy of Mars (Richardson and Wilson, 2002) might be, in the long term, a more robust climate phenomenon rather than GDS, likely affected by changing obliquity of the planet (Laskar, 2004).

Overall, our results cannot be easily reconciled with water values inferred from NGIMS ion measurements, suggesting the thermosphere hosts much more water during the GDS than during the rest of the year. However, we note that the only time when Stone et al. (2020) reported measurements around perihelion concerned the L_S interval between 240° and 265° of MY33 (Figure 4 of Stone et al., 2020). It showed the same brutal trend as during the onset of the MY34 GDS, with values far exceeding those reported for the regional dust storm of MY32, still a factor of 3 smaller than during the GDS.

Our results remain in line with Fedorova et al. (2020, 2021) conclusion about the perihelion season being the main conveyor of water to high altitudes on a long-term basis. A bridge between the ACS measurements presented here and NGIMS measurements leaves room for an additional or refined photochemical process that could link H_2O relative abundances at 120 km with those inferred from NGIMS at 150 km. Both measurements bring unique constraints in our attempt to understand how the water in the lower atmosphere connects with the escaping hydrogen in the exosphere, an essential step before extrapolating the water escape back in time safely.

Acknowledgments, Samples, and Data

ExoMars is a joint space mission of the European Space Agency (ESA) and Roscosmos. The ACS experiment is led by the Space Research Institute (IKI) in Moscow, assisted by LATMOS in France. Retrievals and analysis of temperature and water distributions in IKI are funded by grant #20-42-09035 of the Russian Science Foundation. The ACS MIR data are available from ESA's Planetary Science Archive at https://archives.esac.esa.int/psa/#!Table%20View/ACS=instrument. The retrieved data with altitude profiles of H_2O VMR for the GDS and perihelion intervals are available at https://data.mendeley.com/datasets/995y7ymdgm/draft?a=daa72362-898d-4c86-8a13-023b4b59134c.

References

Alday, J., Wilson C. F., Irwin, P. G. J., Olsen, K. S., Baggio, L., Montmessin, F., et al. (2019). Oxygen isotopic ratios in Martian water vapour observed by ACS MIR on board the ExoMars Trace Gas Orbiter. *Astronomy and Astrophysics*, *630*, A91. doi:10.1051/0004-6361/201936234.

Alday, J., Trokhimovskiy, A ., Irwin, P. G. J., Wilson, C. F., Montmessin, F., Lefèvre, F., et al. (2021). Photolysis controls the isotopic composition of water products escaping Mars' atmosphere. *Nature Astronomy* (revised version).

Aoki, S., Vandaele, A. C., Daerden, F., Villanueva, G. L., Liuzzi, G., Thomas, I. R., et al. (2019). Water Vapor Vertical Profiles on Mars in Dust Storms Observed by TGO/NOMAD. *Journal of Geophysical Research: Planets*, *124*(12), 3482-3497. doi:10.1029/2019je006109.

Benna, M., Mahaffy, P. R., Grebowsky, J. M., Fox, J. L., Yelle, R. V., & Jakosky, B. M. (2015). First measurements of composition and dynamics of the Martian ionosphere by MAVEN's Neutral Gas and Ion Mass Spectrometer. *Geophysical Research Letters*, *42*, 8958–8965, doi:10.1002/2015GL066146.

Chaffin, M., Deighan, J., Schneider, N., & Stewart, A. (2017). Elevated atmospheric escape of atomic hydrogen from Mars induced by high-altitude water. Nature Geoscience, 10(3), 174. doi:10.1038/ngeo2887.

Clancy, R. T., Grossman, A. W., Wolff, M. J., James, P. B., Rudy, D. J., Billawala, Y. N., et al. (1996). Water vapor saturation at low altitudes around Mars aphelion: A key to Mars climate? *Icarus*, *122*(1), 36-62. doi:10.1006/icar.1996.0108.

Fedorova, A., Bertaux, J.-L., Betsis, D., Montmessin, F., Korablev, O., Maltagliati, L., & Clarke, J. (2018). Water vapor in the middle atmosphere of Mars during the 2007 global dust storm. Icarus, 300, 440–457.

Fedorova, A. A., Montmessin, F., Korablev, O., Luginin, M., Trokhimovskiy, A., Belyaev, D. A., et al. (2020). Stormy water on Mars: The distribution and saturation of atmospheric water during the dusty season. *Science*, *367*(6475), 297-300. doi:10.1126/science.aay9522.

Fedorova, A., Montmessin, F., Korablev, O., Lefèvre, F., Trokhimovskiy, A., & Bertaux, J. L. (2021). Multi-annual monitoring of the water vapor vertical distribution on Mars by SPICAM on Mars Express. *Journal of Geophysical Research: Planets*, *126*, e2020JE006616. doi:10.1029/2020JE006616.

Fox, J. L., Benna, M., Mahaffy, P. R., & Jakosky B. M. (2015). Water and water ions in the Martian thermosphere/ionosphere. *Geophysical Research Letters*, *42*, 8977–8985, doi:10.1002/2015GL065465.

Gamache, R. R., Farese, M., & Renaud, C. L. (2016). A spectral line list for water isotopologues in the 1100–4100 cm-1 region for application to CO_2-rich planetary atmospheres. *Journal of Molecular Spectroscopy*, *326*, 144-150. doi:10.1016/j.jms.2015.09.001.

Gordon, I. E., Rothman, L. S., Hill, C., Kochanov, R. V., Tan, Y., Bernath, P. F., et al. (2017). The HITRAN2016 molecular spectroscopic database. *Journal of Quantum Spectroscopy and Radiative Transfer*, *203*, 3–69. doi:10.1016/j.jqsrt.2017.06.038.

Heavens, N. G., Kleinböhl, A., Chaffin, M. S., Halekas, J. S., Kass, D. M., Hayne, P. O., et al. (2018). Hydrogen escape from Mars enhanced by deep convection in dust storms. *Nature Astronomy*, *2*(2), 126-132. doi:10.1038/s41550-017-0353-4

Jakosky, B. M. (1985). The seasonal cycle of water on Mars. *Space Science Review, 41,* 131–200. doi:10.1007/BF00241348

Korablev, O. I., Montmessin, F., Trokhimovskiy, A., Fedorova, A. A., Shakun, A. V., Grigoriev, A. V., et al. (2018). The Atmospheric Chemistry Suite (ACS) of Three Spectrometers for the ExoMars 2016 Trace Gas Orbiter. *Space Science Review*, *214*(1). doi:10.1007/s11214-017-0437-6

Krasnopolsky, V. A. (2002). Mars' upper atmosphere and ionosphere at low, medium, and high solar activities: implications for evolution of water. *Journal of Geophysical Research*, *107*(E12), 5128. doi:10.1029/2001JE001809.

Krasnopolsky, V. A. (2015). Variations of the HDO/H2O ratio in the martian atmosphere and loss of water from Mars. *Icarus, 257,* 377–386. doi:10.1016/j.icarus.2015.05.021.

Krasnopolsky, V. A. (2019). Photochemistry of water in the martian thermosphere and its effect on hydrogen escape. *Icarus*, *321*, 62–70. doi:10.1016/j.icarus.2018.10.033.

Laskar, J., Correia, A.C.M., Gastineau, M., Joutel, F., Levrard, B., Robutel, P. (2004). Long term evolution and chaotic diffusion of the insolation quantities of Mars. *Icarus*, *170*(2), 343-364. doi:10.1016/j.icarus.2004.04.005.

Malathy Devi, V., Benner, D. C., Sung, K., Crawford, T. J., Gamache, R. R., Renaudc, C. L., et al. (2017). Line parameters for CO_2- and self-broadening in the ν3 band of $HD^{16}O$. *Jouranal of Quantum Spectroscopy and Radiative Transfer*, *203*, 158–174. doi:10.1016/j.jqsrt.2017.02.020.

Maltagliati, L., Montmessin, F., Korablev, O., Fedorova, A., Forget, F., Määttänen, A., Lefèvre, F., & Bertaux, J.-L. (2013). Annual survey of water vapor vertical distribution and water–aerosol coupling in the martian atmosphere observed by SPICAM/MEx solar occultations. *Icarus*, *223*, 942–962. doi:10.1016/j.icarus.2012.12.012.

Marquardt, D. (1963). An Algorithm for Least-Squares Estimation of Nonlinear Parameters". SIAM. *Journal on Applied Mathematics*, *11*(2), 431–441. doi:10.1137/0111030.

Millour, E., Forget, F., Spiga, A., Vals, M., Zakharov, V., Montabone, L., et al. (2018). *The Mars Climate Database (version 5.3)*. Paper presented at the Mars Science Workshop "From Mars Express to ExoMars", held 27-28 February 2018 at ESAC, Madrid, Spain, id.68. https://www.cosmos.esa.int/web/mars-science-workshop-2018.

McElroy, M. B., & Donahue, T. M. (1972). Stability of the Martian atmosphere. *Science*, *177*(4053), 986-8 986. doi:10.1126/science.177.4053.986.

Montabone, L., Spiga, A., Kass, D. M., Kleinböhl, A., Forget, F., & Millour, E. (2020). Martian Year 34 column dust climatology from Mars Climate Sounder observations: Reconstructed maps and model simulations. *Journal of Geophysical Research: Planets*, *125*(8), e06111. doi:10.1029/2019JE006111.

Owen, T., Maillard, J. P., de Bergh, C., & Lutz, B. L. (1988). Deuterium on Mars: The abundance of HDO and the value of D/H. *Science, 240*, 1767–1770. doi:10.1126/science.240.4860.1767.

Richardson, M. I., & Wilson, R. J. (2002). Investigation of the nature and stability of the Martian seasonal water cycle with a general circulation model. *Journal of Geophysical Research*, *107*(E5), 5031, doi:10.1029/2001JE001536.

Rodin, A. V., Korablev, O. I., & Moroz, V. I. (1997). Vertical distribution of water in the near-equatorial troposphere of Mars: water vapor and clouds. *Icarus*, *125*(1), 212-229. doi:10.1006/icar.1996.5602.

Shaposhnikov, D. S., Medvedev, A. S., Rodin, A. V., & Hartogh, P. (2019). Seasonal water "pump" in the atmosphere of mars: Vertical transport to the thermosphere. *Geophysical Research Letters*, *46*, 4161–4169. doi:10.1029/2019GL082839.

Stone, W., Yelle, R. V., Benna, M., Lo, D. Y., Elrod, M. K., & Mahaffy P. R. (2020). Hydrogen escape from Mars is driven by seasonal and dust storm transport of water. *Science*, *370*(6518), 824–831. doi:10.1126/science.aba5229.

Villanueva, G. L., Liuzzi, G., Crismani, M. M. J., Aoki, S., Vandaele, A. C., et al. (2021). Water heavily fractionated as it ascends on Mars as revealed by ExoMars/NOMAD. *Science Advances*, *7*(7), eabc8843. doi:10.1126/sciadv.abc8843.

Wang, H., & Richardson, M. I. (2015). The origin, evolution, and trajectory of large dust storms on Mars during Mars years 24-30 (1999-2011). *Icarus*, *251*, 112-127. doi:10.1016/j.icarus.2013.10.033.

Zurek, R. W. & Martin, L. J. (1993). Interannual variability of planet-encircling dust storms on Mars. *Journal of Geophysical Research*, *98*(E2), 3247-3259. doi:10.1029/92JE02936.